



# Structural, morphological, and temperature-tuned bandgap properties of single-step thermally evaporated $\text{Sb}_2\text{Se}_3$ thin films

M. Terlemezoglu<sup>1</sup>

Received: 6 February 2024 / Accepted: 22 March 2024 / Published online: 28 March 2024  
© The Author(s) 2024

## Abstract

In this study, antimony selenide ( $\text{Sb}_2\text{Se}_3$ ) thin films were deposited on a glass substrate through a single-step thermal evaporation process, employing sintered powder as a source material. A detailed investigation of the structural, morphological, and temperature-dependent optical properties of fabricated thin films was performed. The X-ray diffraction (XRD) pattern indicated the presence of the  $\text{Sb}_2\text{Se}_3$  phase, characterized by an orthorhombic crystalline structure. Examination through scanning electron microscopy (SEM) revealed a fully covered, void-free, and densely packed morphology on the thin film surface. Raman spectrum of the film showed the vibrational characteristics of  $\text{Sb}_2\text{Se}_3$ . Transmission spectra of  $\text{Sb}_2\text{Se}_3$  thin film were measured at various temperatures within the range of 10–300 K. The analysis of these measurements demonstrated that optical bandgap energy decreases from 1.28 to 1.25 eV as increasing temperature from 10 to 300 K. The variation of bandgap with temperature was accurately characterized by Varshni and Bose–Einstein relations to elucidate bandgap at 0 K, rate of change of bandgap, and Debye temperature. These findings in this study may be useful for advancing the development of  $\text{Sb}_2\text{Se}_3$  film-based solar cell technology and its applications in optoelectronics.

**Keywords** Antimony selenide · Thermal evaporation · Chalcogenides

## 1 Introduction

Over the last few decades, solving the problems of environmental pollution, energy shortage, and global warming has been a global priority [1]. Photovoltaic technology is one of the most promising clean and sustainable renewable energy sources to tackle these problems [2]. In the photovoltaic market, crystalline silicon solar cells, copper indium gallium selenide (CIGS), cadmium telluride (CdTe), and perovskites solar cells are the leading materials having remarkable device efficiencies of over 20% [3, 4]. However, the indirect bandgap of silicon, the scarcity of gallium (Ga) and indium (In) elements, the toxicity of cadmium (Cd), and the instability of perovskites solar cells are the constraints for the mass production of the PV industry [4]. Recently, kesterite materials such as  $\text{Cu}_2\text{ZnSn}(\text{S},\text{Se})_4$  (CZTSSe) have been explored by researchers as an alternative material to

overcome these problems. CZTSSe having earth-abundant and non-toxic elements has similar optoelectronic properties to CIGS materials [3, 5–9]. However, due to the complex structure of this material, undesired secondary phases are easily formed during the fabrication process. This prevents the commercialization and production of high-efficiency CZTSSe solar cells. Indeed, so far, the record efficiency of CZTSSe thin film-based solar cells is %12.6 through the hydrazine-based solution [10]. Hence, nowadays, antimony selenide ( $\text{Sb}_2\text{Se}_3$ ) with a simple binary composition and high optical absorption ( $> 10^5 \text{ cm}^{-1}$  in the visible region) is an attractive candidate for solar cell absorber material.  $\text{Sb}_2\text{Se}_3$  belonging to the  $A_m^V B_n^{VI}$  group crystalizes in the orthorhombic configuration of the Pnma (62) space group [11]. In addition, it has a direct bandgap energy of 1.0–1.3 eV which is close to the theoretically ideal bandgap value for the absorber layer of solar cells [2, 12].  $\text{Sb}_2\text{Se}_3$  semiconductor thin films are important not only for the photovoltaic industry [13, 14] but also for comprehensive applications such as nonvolatile electronic memory [15], optical recording material [16, 17], thermoelectric devices [18], and switching [19].

Many methods for the fabrication of  $\text{Sb}_2\text{Se}_3$  thin films have been proposed so far including radio frequency (RF)

✉ M. Terlemezoglu  
tmakbule@gazi.edu.tr; terlemezoglu.m@gmail.com

<sup>1</sup> Department of Physics, Faculty of Science, Gazi Üniversitesi Emniyet Mahallesi, Bandırma Caddesi No: 6/8, Yenimahalle, 06500 Ankara, Turkey

magnetron sputtering [2], thermal evaporation [20], electro-deposition [21], spray pyrolysis [22], chemical bath deposition [23], and spin coating [24]. Among these methods, thermal evaporation is a cost-effective approach, and it is suitable for large-scale mass production. Among these methods, thermal evaporation is a preferred method for fabricating antimony selenide thin films due to several key advantages. Firstly,  $\text{Sb}_2\text{Se}_3$  has a relatively low evaporation temperature, which makes thermal evaporation a suitable technique to achieve controlled and uniform film thickness without degrading the material's intrinsic properties. This method allows for high-purity films since it involves physical vapor deposition in a vacuum, minimizing contamination and enabling the growth of stoichiometric films which are crucial for semiconductor applications. Additionally, thermal evaporation offers excellent control over the deposition rate and thickness, which are critical parameters for tuning the optical and electrical properties of  $\text{Sb}_2\text{Se}_3$  films for photovoltaic and thermoelectric applications. The simplicity and scalability of the thermal evaporation process further contribute to its selection for  $\text{Sb}_2\text{Se}_3$  fabrication, facilitating the development of cost-effective and efficient manufacturing processes for devices based on this promising material [25–29]

This study primarily focuses on fabricating high-quality  $\text{Sb}_2\text{Se}_3$  thin films in a cost-effective manner by excluding additional deposition steps like the selenization process and by also examining the temperature dependency of the optical bandgap of produced thin films. For this reason,  $\text{Sb}_2\text{Se}_3$  thin films were fabricated through thermal evaporation in a single step using sintered powder. The structural and morphological properties of deposited thin films were studied in detail. Then, the temperature-dependent bandgap characteristics of deposited  $\text{Sb}_2\text{Se}_3$  films were investigated by Varshni and Bose–Einstein relation using transmittance spectra. This study innovates by simplifying the fabrication of high-quality  $\text{Sb}_2\text{Se}_3$  thin films, crucial for photovoltaic applications, by using a cost-effective, single-step thermal evaporation process without additional selenization steps. It thoroughly investigates the structural and morphological characteristics of these films and examines their temperature-dependent optical bandgaps through Varshni and Bose–Einstein relations. This approach could significantly impact semiconductor research by offering insights into material behavior under various temperatures and streamlining production processes.

## 2 Experimental details

$\text{Sb}_2\text{Se}_3$  thin films were coated on  $2 \times 2 \text{ cm}^2$ , 4 mm thick, soda lime glass (SLG) substrates by a thermal evaporation system in a single-step process. The stoichiometric sintered powder which was prepared by highly pure materials Se (99.99%)

and Sb (99.999%) was utilized as a deposition source. The sintering process relies on the reaction of constituent elements having high purity at a temperature above their melting points within a sealed quartz crucible under vacuum conditions. In the evaporation process, the sintered powder was placed into a thermal boat and situated below 15 cm of the substrate holder. The base pressure of the system was around  $1 \times 10^{-6}$  Torr and deposition temperature was held at  $150^\circ\text{C}$  since it was observed that this substrate temperature was the minimum required temperature value to obtain the polycrystalline nature of deposited film. Both the thickness of the film and evaporation rate were controlled in situ by an Inficon XTM/2 deposition/thickness monitor. They were adjusted to be 900 nm and 2–3 Å/s, respectively. Following the deposition process, the thickness of the films was confirmed by the Veeco Dektak 6 M stylus profilometer.

The deposited thin films were characterized by structural, morphological, and optical analysis techniques. X-ray diffraction (XRD) measurement was used to ascertain the properties of the crystal structure of samples (XRD, Rigaku Miniflex diffractometer with  $\lambda = 0.154 \text{ nm}$   $\text{CuK}\alpha$  radiation source). The elemental composition and surface morphology of samples were conducted by scanning electron microscope (SEM, Zeiss EVO15) equipped with energy dispersive X-ray analysis (EDXA). Raman scattering spectrum was performed in the frequency range of  $100\text{--}250 \text{ cm}^{-1}$  (Horiba-Jobin Yvon iHR550 imaging spectrometer). Transmittance measurements of the samples were obtained at various temperatures (Jenway 6400 model spectrophotometer) in which the sample was placed into a closed cycle helium cryostat (Advanced Research Systems, Model CSW-202) attached with a temperature controller (Lakeshore Model 331).

## 3 Results and discussions

To elucidate the structural analysis of deposited films, XRD and Raman spectroscopy were performed. The XRD measurement of the samples was done in the  $2\theta$  angle range of  $10^\circ\text{--}50^\circ$ . As shown in Fig. 1, strong diffraction peaks conforming to a polycrystalline nature were detected in the XRD pattern of the coated films on SLG. It was also obtained that films crystallize in the orthorhombic structure of  $\text{Sb}_2\text{Se}_3$  (JCPDS 00-015-0861), which belongs to the  $\text{Pmna}$  62 space group. All diffraction peaks observed in the XRD pattern were labeled to clarify Fig. 1. The lattice parameters were determined to be approximately  $a = 11.1 \text{ \AA}$ ,  $b = 3.9 \text{ \AA}$ , and  $c = 11.6 \text{ \AA}$ , aligning closely with the values reported in the literature [30, 31].

Raman spectroscopy was employed for the characterization of the deposited film since it is a well-known, non-destructive technique for identifying both primary and impurity phases. Figure 2 presents the Raman spectrum of

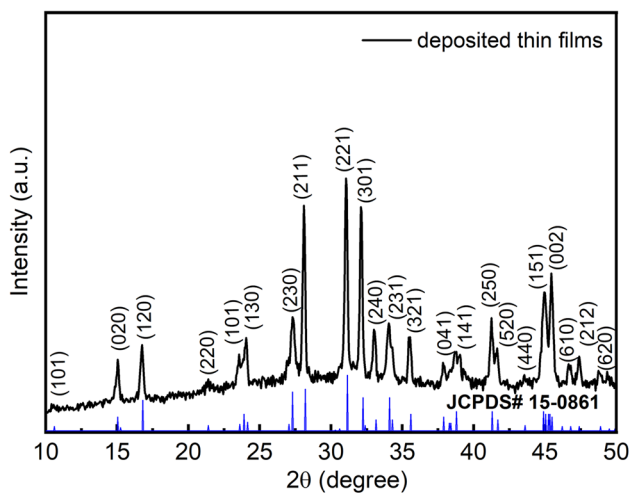


Fig. 1 XRD spectrum of deposited  $\text{Sb}_2\text{Se}_3$  thin films

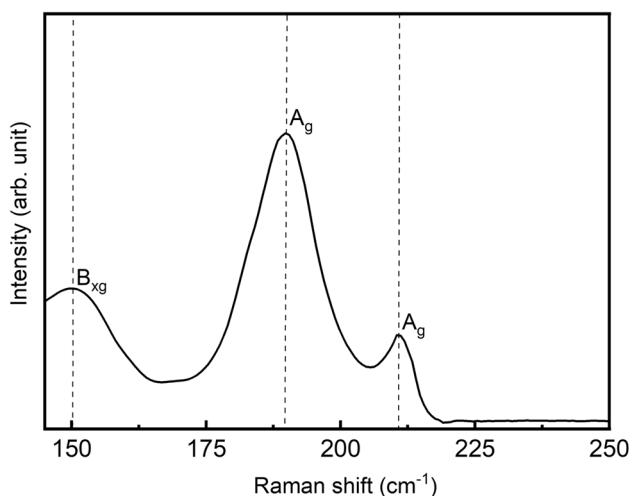


Fig. 2 Raman spectrum of deposited  $\text{Sb}_2\text{Se}_3$  thin films

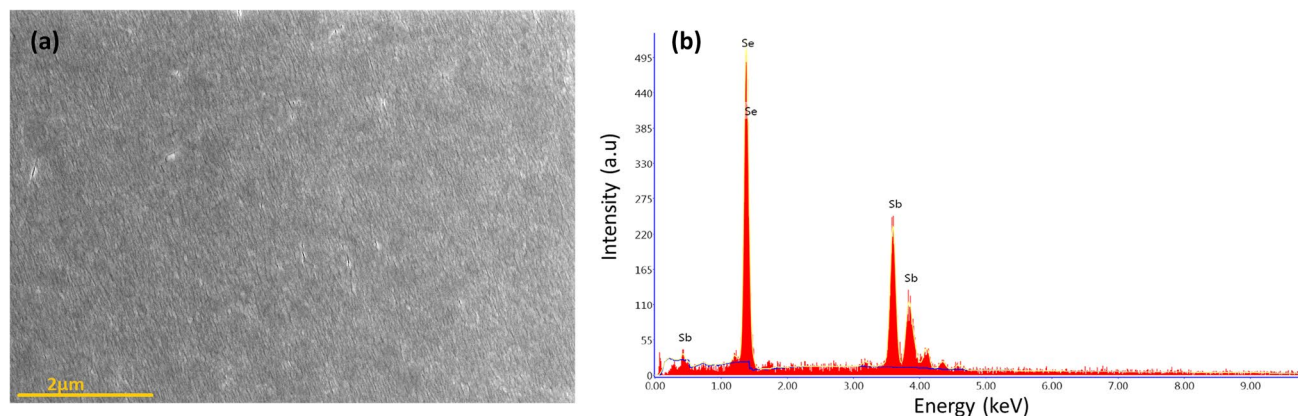
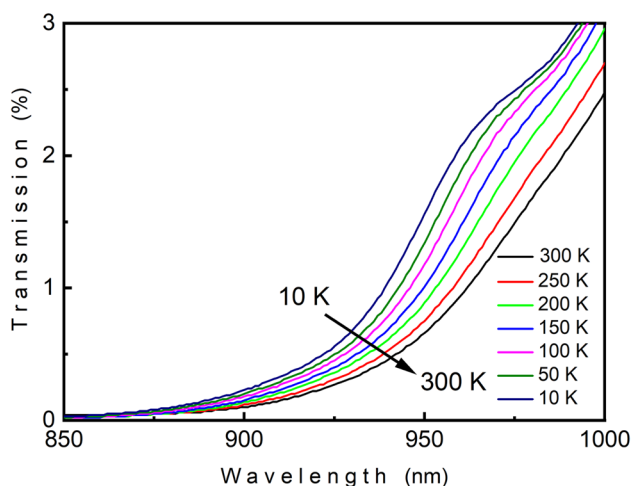


Fig. 3 SEM micrograph (a) and EDS spectrum (b) of  $\text{Sb}_2\text{Se}_3$  thin films

the deposited films. In this figure, the prominent peak centered at  $189\text{ cm}^{-1}$  is the characteristic peak of the Sb–Se stretching mode, labeled as  $A_g$  mode. The peak centered at  $150\text{ cm}^{-1}$  is identified as the  $B_{xg}$  mode, which is characteristic of the Sb–Sb bond in the Raman spectrum. Additionally, the centered peak at  $211\text{ cm}^{-1}$  is associated with Se–Se bonds, assigned to  $A_g$  mode. All spectrum of deposited film is compatible with the reported studies in the literature. [32, 33]. The dashed lines in Fig. 2 are the peak positions of the data given in [33].

The surface morphology of the deposited films was examined through SEM imaging. Figure 3a illustrates the surface morphology of the sample on SLG. It was clearly seen that the surface of the deposited thin film has a dense packet morphology with small grains. The EDS measurement provided the elemental composition analysis of the deposited films. The atomic percentage ratios for Sb and Se were determined as 42% and 58%, respectively (as given in Fig. 3b).

The bandgap properties of  $\text{Sb}_2\text{Se}_3$  thin film were explored by conducting transmission experiments at different temperatures. The transmittance (T) spectra of fabricated thin films within the high absorption range are depicted in Fig. 4. A shift to lower wavelengths with increasing temperature was observed in the spectra. This observed shift indicates that the bandgap energy of  $\text{Sb}_2\text{Se}_3$  thin films increases as the temperature decreases, which aligns with the theoretical expectations [34]. Temperature–bandgap relation in a semiconductor material is elucidated by electron–phonon interaction [35]. The theoretical studies revealed that exciton energies increase with decreasing temperature, and a similar correlation occurs in the bandgap behavior. On the other hand, alternatively, the relationship between temperature and bandgap energy is explained by considering the interatomic distance between atoms, resulting in a decrease in the periodic potential well for electrons within the lattice. Consequently, the bandgap of a semiconductor material decreases with increasing temperature.



**Fig. 4** Temperature-dependent transmittance spectra of deposited  $Sb_2Se_3$  thin films around the absorption edge

The absorption coefficient ( $\alpha$ ), was determined through the relationship with transmittance as follows [36],

$$\alpha = \frac{1}{d} \ln(T) \tag{1}$$

where  $d$  is the film thickness which was measured as 900 nm nearly.

The absorption coefficient was determined to be in the order of  $10^5 \text{ cm}^{-1}$  in the visible region, indicating its consistency with the values reported in the literature [37]. The optical bandgap energy ( $E_g$ ) of thin films at different ambient temperatures was extracted from the absorption spectra around the absorption edge using the Tauc’s relation, expressed as follow [34],

$$(\alpha h\nu) = A(h\nu - E_g)^m \tag{2}$$

where  $A$  is constant,  $h\nu$  is the energy of the incident photon, and  $m = 1/2$  (or 2) for direct (or indirect) transition. The optical bandgaps were determined by extrapolating the linear part of the  $(\alpha h\nu)^2$  vs  $h\nu$  plot to the energy axis [38, 39]. Figure 5 represents the plots of  $(\alpha h\nu)^2$  vs.  $h\nu$  at 10 K and 300 K. Only limit temperatures were given in Fig. 5 so that the reader can easily see the shift of the bandgap. The spectrum of  $Sb_2Se_3$  thin film at 300 K revealed the direct bandgap of 1.25 eV, as determined by the linear fit. This shows that produced films are well-suited for various applications, including solar cells and heterojunction diodes. At the lowest applied temperatures of 10 K, the bandgap energy of  $Sb_2Se_3$  increased to 1.28 eV. The temperature dependence bandgap energy as a function of temperature is depicted in Fig. 6. In the literature, various models have been used to describe the  $E_g$ - $T$  relationship [40–43]. In this study, the  $E_g$ - $T$  relation of fabricated films was examined using two

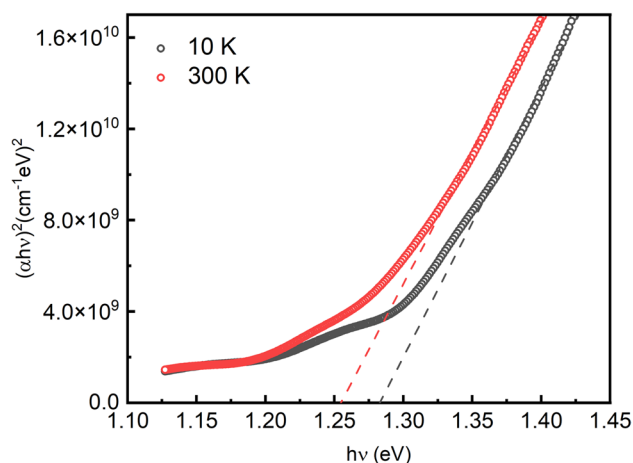


**Fig. 5** Plots of  $(\alpha h\nu)^2$  vs.  $h\nu$  at 10 K and 300 K. The dashed line shows the linear fit for the Tauc method

established models, namely the Varshni and Bose–Einstein models. The empirical Varshni model characterizes the relationship between bandgap energy and temperature through the following function [44],

$$E_g(T) = E_g(0) - \gamma \frac{T^2}{T + \Theta_D} \tag{3}$$

where  $E_g(0)$ ,  $\gamma$  and  $\Theta_D$  represent the bandgap at absolute zero temperature, rate of change of bandgap with temperature and Debye temperature, respectively.

The analysis of  $E_g$ – $T$  dependency depicted in Fig. 6 yielded the following optical values:  $E_g(0) = 1.28 \text{ eV}$ ,  $\gamma = 0.205 \text{ meV/K}$  and  $\Theta_D = 362 (\pm 31) \text{ K}$ . The variation of  $E_g$ – $T$  was further investigated by considering the

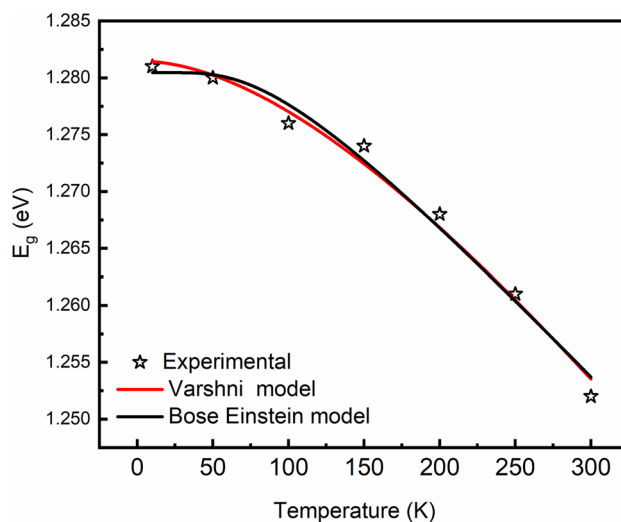


**Fig. 6** Temperature-dependent bandgap energies of fabricated  $Sb_2Se_3$  thin films. Solid lines represent the fits based on Eqs. (3) and (4)

semiempirical Bose–Einstein model, expressed as follows [45, 46],

$$E_g(T) = E_g(0) + \gamma \frac{\Theta_E}{e^{\Theta_E/T} - 1} \quad (4)$$

where  $\Theta_E$  represents Einstein temperature, with the relationship defined as  $\Theta_D = 4\Theta_E/3$ . In Fig. 6, the fitted line based on the Bose–Einstein model demonstrated successful fitting yielding, the optical values:  $E_g(0) = 1.28$  eV,  $\gamma = 0.143$  meV/K and  $\Theta_D = 356 (\pm 36)$  K. The analysis demonstrated that the error rates for  $E_g(0)$  and  $\gamma$  parameters in both models were remarkably low. Conversely,  $\Theta_D$  and  $\Theta_E$  are the non-dominant parameters in Eqs. (3) and (4), respectively. Consequently, even minor variations in the bandgap energy can significantly impact these parameters. This leads to notably higher error rates for Debye temperature in both models when compared to other parameters. Considering these error rates, there is noticeable consistency observed between the obtained values of Debye temperature. Furthermore, the obtained values for the Debye temperature are in accordance with the previously reported study, identified as 358 K in the literature [42].

## 4 Conclusion

In summary, this study presents the findings regarding the structural, morphological, and temperature-dependent optical properties of  $\text{Sb}_2\text{Se}_3$  thin films fabricated through a one-step thermal evaporation process. The formation of a single-phase nature of  $\text{Sb}_2\text{Se}_3$  thin films was confirmed by XRD and Raman spectroscopy. The compositional analysis indicated that the deposited thin films exhibit the desired stoichiometry. The compositional analysis indicated that the deposited thin films exhibit the desired stoichiometry. The transmission spectra of the  $\text{Sb}_2\text{Se}_3$  thin films were recorded at different temperatures ranging from 10 to 300 K. The analysis of these measurements revealed a decrease in optical bandgap energy from 1.28 eV to 1.25 eV as the temperature increased. The relationship between temperature and optical bandgap was well described by using both the Varshni and Bose–Einstein expressions. According to Varshni model analyses, the optical parameters were determined as  $E_g(0) = 1.28$  eV,  $\gamma = 0.205$  meV/K and  $\Theta_D = 362 (\pm 31)$  K. On the other hand, the Bose–Einstein model yielded  $E_g(0) = 1.28$  eV,  $\gamma = 0.143$  meV/K and  $\Theta_D = 356 (\pm 36)$  K. This research could contribute to progress of  $\text{Sb}_2\text{Se}_3$  based solar cell technology and its utilization in optoelectronics.

**Author contributions** Makbule Terlemezoglu: Conceptualization, Methodology, Formal analysis, Investigation, Writing—Original Draft.

**Funding** Open access funding provided by the Scientific and Technological Research Council of Türkiye (TÜBİTAK).

**Data and code availability** Data will be made available on request.

## Declarations

**Conflict of interest** The authors declare that they have no known competing financial interests or personal relationships that could have appeared to influence the work reported in this paper.

**Ethical approval** Not applicable.

**Open Access** This article is licensed under a Creative Commons Attribution 4.0 International License, which permits use, sharing, adaptation, distribution and reproduction in any medium or format, as long as you give appropriate credit to the original author(s) and the source, provide a link to the Creative Commons licence, and indicate if changes were made. The images or other third party material in this article are included in the article's Creative Commons licence, unless indicated otherwise in a credit line to the material. If material is not included in the article's Creative Commons licence and your intended use is not permitted by statutory regulation or exceeds the permitted use, you will need to obtain permission directly from the copyright holder. To view a copy of this licence, visit <http://creativecommons.org/licenses/by/4.0/>.

## References

1. Y. zhen Li, F. Li, G. xing Liang, W. liang Zheng, Y. min Xu, Z. hao Zheng, P. Fan, Surf. Coatings Technol. **358**, 1013 (2019)
2. A. Shongalova, M.R. Correia, J.P. Teixeira, J.P. Leitão, J.C. González, S. Ranjbar, S. Garud, B. Vermang, J.M.V. Cunha, P.M.P. Salomé, P.A. Fernandes, Sol. Energy Mater. Sol. Cells **187**, 219 (2018)
3. X. Liu, J. Chen, M. Luo, M. Leng, Z. Xia, Y. Zhou, S. Qin, D. Xue, L. Lv, H. Huang, D. Niu, and J. Tang, (2014).
4. S. Ghosh, M.V.B. Moreira, C. Fantini, J.C. González, Sol. Energy **211**, 613 (2020)
5. M. Terlemezoglu, Ö. Bayraklı, H.H. Güllü, T. Çolakoğlu, D.E. Yıldız, M. Parlak, J. Mater. Sci. Mater. Electron. **29**, 5264 (2018)
6. M. Terlemezoglu, Ö. Bayraklı Sürücü, T. Çolakoğlu, M.K. Abak, H.H. Güllü, Ç. Erçelebi, M. Parlak, Mater. Res. Express **6**, 026421 (2018)
7. Ö. Bayraklı, M. Terlemezoglu, H.H. Güllü, M. Parlak, J. Alloys Compd. **709**, 337 (2017)
8. Ö. Bayraklı, M. Terlemezoglu, H.H. Güllü, M. Parlak, Mater. Res. Express **4**, 086411 (2017)
9. M. Terlemezoglu, Ö. Bayraklı Sürücü, C. Dogru, H.H. Güllü, E.H. Ciftpinar, Ç. Erçelebi, M. Parlak, J. Mater. Sci. Mater. Electron. **30**, 11301 (2019)
10. W. Wang, M.T. Winkler, O. Gunawan, T. Gokmen, T.K. Todorov, Y. Zhu, D.B. Mitzi, Adv. Energy Mater. **4**, 1 (2014)
11. C. Chen, W. Li, Y. Zhou, C. Chen, M. Luo, X. Liu, K. Zeng, B. Yang, C. Zhang, J. Han, J. Tang, Appl. Phys. Lett. **107**, 043905 (2015)
12. Y. Lai, Z. Chen, C. Han, L. Jiang, F. Liu, J. Li, Y. Liu, Appl. Surf. Sci. **261**, 510 (2012)
13. Z. Li, H. Zhu, Y. Guo, X. Niu, X. Chen, C. Zhang, W. Zhang, X. Liang, D. Zhou, J. Chen, Y. Mai, Appl. Phys. Express **9**, 052302 (2016)
14. B.R. Sankapal, C.D. Lokhande, Sol. Energy Mater. Sol. Cells **69**, 43 (2001)

15. T. Wu, G. Wang, A. Lotnyk, J. Zhu, Y. Jiao, X. Shen, *Appl. Phys. Lett.* **123**, 073102 (2023)
16. S. Jayakumar, C. Balasubramanian, S.K. Narayandass, D. Mangalaraj, C.P.G. Vallabhan, *Thin Solid Films* **266**, 62 (1995)
17. Y. Nakane, N. Sato, H. Makino, and S. Miyaoka, **0529**, 76 <https://doi.org/10.1117/12.946435> (1985)
18. H.C. Kim, T.S. Oh, D.B. Hyun, *J. Phys. Chem. Solids* **61**, 743 (2000)
19. C. Liu, Y. Yuan, L. Cheng, J. Su, X. Zhang, X. Li, H. Zhang, M. Xu, J. Li, *Results Phys.* **13**, 102228 (2019)
20. E.A. El-Sayad, *J. Non Cryst. Solids* **354**, 3806 (2008)
21. A.P. Torane, C.H. Bhosale, *J. Phys. Chem. Solids* **63**, 1849 (2002)
22. K.Y. Rajpure, C.H. Bhosale, *Mater. Chem. Phys.* **62**, 169 (2000)
23. Y. Rodríguez-Lazcano, Y. Peña, M.T.S. Nair, P.K. Nair, *Thin Solid Films* **493**, 77 (2005)
24. Y.C. Choi, T.N. Mandal, W.S. Yang, Y.H. Lee, S.H. Im, J.H. Noh, S. Il Seok, *Angew. Chem.* **126**, 1353 (2014)
25. S. Yao, J. Wang, J. Cheng, L. Fu, F. Xie, Y. Zhang, L. Li, A.C.S. *Appl. Mater. Interfaces* **12**, 24112 (2020)
26. Y.M. Zhong, M. Ishaq, M.Y. Nie, Y.X. Chen, S. Chen, J.T. Luo, P. Fan, Z.H. Zheng, G.X. Liang, *Ceram. Int.* **49**, 36935 (2023)
27. C. Chen, K. Li, J. Tang, *Sol. RRL* **6**, 2200094 (2022)
28. V. Kumar, E. Artegiani, A. Kumar, G. Mariotto, F. Piccinelli, A. Romeo, *Sol. Energy* **193**, 452 (2019)
29. L. Zhang, K. Wu, J. Yu, Y. Yu, Y. Wei, *Vacuum* **183**, 109840 (2021)
30. A. Mavlonov, T. Razykov, F. Raziq, J. Gan, J. Chantana, Y. Kawano, T. Nishimura, H. Wei, A. Zakutayev, T. Minemoto, X. Zu, S. Li, L. Qiao, *Sol. Energy* **201**, 227 (2020)
31. R. Caracas, X. Gonze, *Phys Chem Minerals* **32**, 295 (2005)
32. N. Fleck, T.D.C. Hobson, C.N. Savory, J. Buckeridge, T.D. Veal, M.R. Correia, D.O. Scanlon, K. Durose, F. Jäckel, *J. Mater. Chem. A* **8**, 8337 (2020)
33. M. Delaney, I. Zeimpekis, D. Lawson, D.W. Hewak, O.L. Muskens, *Adv. Funct. Mater.* **30**, 1 (2020)
34. J. I. Pankove, *Dover Publ. Inc.* **119**, 450 (1975).
35. J. Bhosale, A.K. Ramdas, A. Burger, A. Muñoz, A.H. Romero, M. Cardona, R. Lauck, R.K. Kremer, *Phys. Rev. B Condens. Matter Mater. Phys.* **86**, 195208 (2012)
36. M. Terlemezoglu, O. Surucu, M. Isik, N. M. Gasanly, M. Parlak, *Appl. Phys. A* **128**, 50 (2022)
37. S. Chen, X. Qiao, Z. Zheng, M. Cathelinaud, H. Ma, X. Fan, X. Zhang, *J. Mater. Chem. C* **6**, 6465 (2018)
38. M. Isik, M. Terlemezoglu, S. Isik, K. Erturk, N.M. Gasanly, *J. Mater. Sci. Mater. Electron.* **32**, 25225 (2021)
39. K. Erturk, M. Isik, M. Terlemezoglu, N.M. Gasanly, *Opt. Mater. (Amst.)* **114**, 110966 (2021)
40. O. Surucu, M. Isik, N.M. Gasanly, M. Terlemezoglu, M. Parlak, *Mater. Lett.* **275**, 128080 (2020)
41. F.I.M. Al-Attar, N. Goyal, S.K. Tripathi, F.I. Mustafa, S. Gupta, N. Goyal, *Artic. J. Optoelectron. Adv. Mater.* **11**, 2019 (2009)
42. M. Birkett, W.M. Linhart, J. Stoner, L.J. Phillips, K. Durose, J. Alaria, J.D. Major, R. Kudrawiec, T.D. Veal, *APL Mater.* **6**, 84901 (2018)
43. M. Isik, N. Gasanly, *Mat. Chem. Phys.* **190**, 74 (2017)
44. Y.P. Varshni, *Physica* **34**, 149 (1967)
45. K.P. O'Donnell, X. Chen, *Appl. Phys. Lett.* **58**, 2924 (1991)
46. M. Isik, M. Terlemezoglu, N. Gasanly, M. Parlak, *Phys. E Low-Dimens. Syst. Nanostruct.* **144**, 115407 (2022)

**Publisher's Note** Springer Nature remains neutral with regard to jurisdictional claims in published maps and institutional affiliations.